Mechanisms underlying the cell-matrixed nerve grafts repairing peripheral nerve defects

Shanshan Wang [a],[b], Hongkui Wang [a], Panjian Lu [a], Leilei Gong [a], Xiaosong Gu [a],[**], Meiyuan Li [a],[*]

[a] *Key Laboratory of Neuroregeneration of Jiangsu and Ministry of Education, Co-innovation Center of Neuroregeneration, NMPA Key Laboratory for Research and Evaluation of Tissue Engineering Technology Products, Nantong University, Nantong, Jiangsu, 226001, PR China*
[b] *Department of Obstetrics and Gynecology , Affiliated Hospital of Nantong University, Nantong, Jiangsu, 226001, PR China*

ARTICLE INFO

ABSTRACT

Decellularized extracellular matrix (dECM), with its distinct biological properties, has gained significant attention as a natural biomaterial. Leveraging its potentials, we successfully developed a three-dimensional matrix-based oriented nerve graft by encapsulating a fibrous scaffold with multilayered conformationally intact and biologically active human bone marrow mesenchymal stem cell-derived decellularized extracellular matrix (hBMSC-dECM). Convincingly, the hBMSC-dECM group exhibited comparable functional recoveries to the autograft group by postoperative week 12. In the comprehensive analysis, the molecular regulations in the hBMSC-dECM group were more intricate and nuanced compared to the autograft group. Nevertheless, both groups displayed similar molecular regulatory processes in terms of vascularization and extracellular matrix. Notably, the hBMSC-dECM group demonstrated sustained high levels of regulation in axon and myelin regeneration at week 12, while the immunomodulation returned to the normal levels after peaking at week 2. Collectively, our findings illustrated the satisfactory construction of a cell-matrixed nerve graft that established a microenvironment conducive to nerve regeneration, and elucidated the distinct molecular regulation patterns and characteristics associated with different repair modes.

1. Introduction

Peripheral nerve injury is a prevalent clinical condition, which not only greatly diminishes patients' quality of life but also amplifies the economic and societal burden it imposes. Currently, nerve regeneration is presently a significant clinical challenge [1,2]. Although autografts are widely regarded as the most effective method for repairing peripheral nerves, their clinical application is hindered by various limitations such as scarcity of donor source, discrepancies in tissue size and structure, and irreversible nerve damage at the donor site [3]. In view of this, empirical efforts have shifted to create a promising tissue-engineered nerve graft that can restore or improve injured nerves [4–6].

Tissue-engineered nerve grafts represent an organic unity composed of scaffold material, supporting cells, extracellular matrix (ECM), and nerve growth factors. This intricate assemblage serves as a guiding bridge, directing the growth of nerve fibers from the proximal to the distal ends. Moreover, it offers competent mechanical support and safeguards for nascent nerve fibers, while concurrently establishing an optimal microenvironment for nerve regeneration [7–9]. Biocompatible polymer materials, owing to their excellent mechanical properties and processability, stand out as promising candidates. Their structural and property dynamics can be tailored as required, thus rendering them highly suitable for large-scale fabrication [10]. In recent years, the development in nerve graft research involves the fabrication of grafts from biodegradable biomaterials incorporating poly (lactic-*co*-glycolic acid) (PLGA) scaffolds and chitosan-coated conduits [11,12]. They have demonstrated promising outcomes in the repair of peripheral nerve defects, facilitating robust regenerative processes. Nevertheless, these polymer materials still exhibit deficiencies in terms of cellular interaction sites and cell adhesion.

Decellularized extracellular matrix (dECM) has emerged as a promising platform for tissue engineering owing to its unique biomechanical properties and tissue-specific composition of the ECM [13]. The ECM represents a three-dimensional polymer network composed of proteins

and polysaccharides [14]. It possesses a complex array of morphological and structural signals that delicately modulate cellular processes, signal transduction pathways, gene expression profiles, and injury healing mechanisms [15–17]. Through the process of decellularization, these cell cultures retain morphological cues that diligently mimic the native microenvironment, whilst concurrently eliminating most antigenic substances. This ensures an effective blockade against pathogen transmission while preserving the desired geometry and flexibility [18–20]. Furthermore, the deposition of dECM by mesenchymal stem cells holds the potential to rejuvenate both stem cells and primary cells, enhancing their capacity for proliferation and differentiation [21,22]. Notably, bone marrow mesenchymal stem cells (BMSCs) serve as a ubiquitous source of seed cells for tissue engineering applications [23,24], which can be mobilised and recruited to the site of injury, where they exhibit the capacity to either differentiate into the phenotype of damaged cells or facilitate the regeneration of endogenous cells by creating a microenvironment that enhances repair process. The therapeutic potential of these scaffolds is further substantiated by the use of a chitosan/silk scaffold encapsulated with the acellular matrix derived from canine BMSCs. This was employed to repair a 60-mm defect in the sciatic nerve of dogs, resulting in satisfactory functional recuperation [25].

In this study, a three-dimensional cell matrix-based oriented nerve graft was successfully constructed by integrating a PLGA fibrous scaffold with a conformationally intact and biologically active human BMSC derived dECM (hBMSC-dECM). This innovative graft was further combined with a chitosan nerve conduit to enhance its structural integrity and functional properties. We utilized a cell-matrixed nerve graft to bridge a 10-mm defect in the rat sciatic nerve. Through our comprehensively evaluation, we were able to shed light on the intricate differences between the cell-matrixed nerve graft and the autologous nerve graft, while also delving into the molecular mechanisms that govern the repair of nerve defects. By creating a microenvironment that promotes axonal growth, we successfully achieved the ultimate objective of regenerating the nerve and restoring its functionality. Furthermore, we meticulously mapped out the gene expressions and regulatory networks, uncovering the molecular characteristics that drive the key biological processes involved in repairing nerve defects using cell-matrixed nerve grafts. This breakthrough opens up a promising new avenue for treating nerve injuries in clinical settings.

2. Materials and methods

2.1. Preparation of the hBMSC-dECM

Passage 3 hBMSCs (ATCC; PCS-500-012) were seeded into 100-mm culture dishes at a density of 10^5 cells/mL and cultured in a serum-free medium (Biological Industries, Israel) until reaching the cell confluence $\geq$90%. Subsequently, 50 μg/mL ascorbic acid (Sigma, St Louis, MO, USA) was supplemented for 10 days with medium refreshed every 2 days. For decellularization, the sample was rinsed three times in phosphate-buffered saline (PBS), and immersed in sterilized ultrapure water for hypotonic treatment at 37 °C for 10 min. After removing the sterilized ultrapure water, the cell lysate containing 3% Triton X-100 and 2% sodium dodecyl sulfate (Sigma) was added for extraction at 37 °C for 5 min. Following another PBS wash, the obtained hBMSC-dECM sample could be stored at 4 °C for approximately 2 weeks.

2.2. Characterization of the hBMSC-dECM

The hBMSC-dECM was placed onto slides and then treated with 4% glutaraldehyde. This was followed by post-fixation with 1% OsO_4, a process of gradient ethanol dehydration, drying at room temperature, crystallization, and adhesion prior to observation under a Hitachi S–3400 N scanning electron microscope (SEM). The samples were double labeled with primary antibodies (mouse anti-fibronectin antibody, 1:100, rabbit anti-collagen I antibody, 1:250; mouse anti-

fibronectin antibody, 1:100, rat anti-laminin antibody, 1:50; and mouse anti-fibronectin antibody, 1:100, rabbit anti-collagen IV antibody, 1:100), and then incubated with appropriate fluorescently labeled secondary antibodies. All antibodies were obtained from Abcam (Cambridge, UK), and the resultant images were observed under fluorescence microscopy (AxioImager M2, Zeiss, Germany).

2.3. Construction of cell-matrixed nerve graft

In brief, the cell-matrixed nerve grafts (Chinese patent ZL202210982152.0) were constructed from chitosan conduits with an internal diameter of 2 mm, PLGA scaffolds woven from 140 to 160 monofilaments (Jiangsu Yitong Biotechnology Company, Nanjing, China) [11]. A gelatinous membrane-like hBMSC-dECM of approximately 0.12 mm thickness with PLGA as the axis was rolled into 6 to 8 layers and threaded into chitosan conduits to construct cell-matrixed nerve grafts before surgery.

2.4. Preparing a rat model of sciatic nerve defect

Male Sprague-Dawley rats, aged between 8 and 10 weeks and weighting between 200 and 220 g, which were obtained from the Experimental Animal Center of Nantong University (license No. SYXK (Su) 2017–0046), were chosen as the subjects for this study. The rats were divided randomly into three groups: the hBMSC-dECM group, wherein cell-matrixed nerve grafts facilitated repair; the autograft group, repaired via autologous sciatic nerves subject to a 180° rotation; and the sham group, entailing exposure of the sciatic nerve without inducing a defect. Each experimental group (n = 25) was evaluated on postoperative day 1, 3, 7 and week 2, 3, 4, 8, 12. All experimental procedures followed the Guide for the Care and Use of Laboratory Animals issued by the US National Research Council and approved by the Laboratory Animal Management Committee of Jiangsu Province, China. For surgical procedures, all animals were deeply anaesthetized using an intraperitoneally administered compound-anesthetic solution comprising chloral hydrate, magnesium sulfate, pentobarbital sodium, ethanol, and propylene glycol. Skin was shaved and disinfected with iodophor before exposing the sciatic nerve in the mid-left thigh. Approximately 8 mm of the nerve was resected close to the sciatic nerve bifurcation, causing it to retract and form a 10-mm defect. The prepared nerve graft was then sutured into the defect using 8-0 micro sutures, followed by muscle and skin sutures. Post-surgical iodophor disinfection was carried out, and the rats were subsequently accommodated in a specific pathogen-free (SPF) facility.

2.5. Behavioral analysis

To evaluate the integrated function, the gait parameters were recorded and analyzed using CatWalk system [26] (Noldus, Wageningen, Netherlands) at week 12. The sciatic nerve function index (SFI) was calculated and statistically analyzed based on the formula: SFI = 109.5 (ETS-NTS)/NTS-38.3 (EPL-NPL)/NPL+13.3 (EIT-NIT)/NIT-8.8 (where TS is toe spread, PL is print length, IT is intermediate toe spread, and E and N indicate the experimental and normal contralateral hind paws, respectively.). To test mechanical sensitivity, we used the Von Frey test [27] to detect the paw withdrawal threshold. The rats were confined in a tester and their hind plantar of the operated side was stimulated with a prick needle under mildly increasing stimulation force (maximum 200 *g*) until a significant withdrawal of the hind paw on the test side occurred. The tests were conducted at intervals of at least 2 min and the mechanical nociceptive threshold (g) was the mean of three consecutive trials. The Hargreaves radiant heat apparatus [28] (IITC Life Science, USA) was used to test thermal sensitivity, with the basal latency of approximately 10 s and the cut-off time was set at 20 s to avoid thermal injury.

2.6. Electrophysiological test

The rats were subjected to electrophysiological examinations at room temperature. Under intraperitoneal anesthesia, we first shaved and disinfected the skin of the rats' operated side using iodophor, and subsequently exposed the sciatic nerve, inclusive of the bridging segment. Electrical stimuli (10 mA in strength) were applied to the sciatic nerve trunk at the proximal and distal ends of the graft from a portable digital MYTO electrophysiological apparatus, and compound muscle action potential (CMAP) of the gastrocnemius muscle was recorded. The assessments of normal sciatic nerve CMAPs were conducted at the uninjured contralateral side.

2.7. Morphological assessment of the regenerative nerve

At week 12 postoperatively, harvested regenerated nerves were fixed, sectioned, and analyzed. The cross-sections (10-μm thickness) of regenerated nerves in the mid-bridge segment were subject to hematoxylin-eosin (HE) evaluation. These sections were also stained with NF200 and S100 (Sigma), respectively. The macrophages were stained with CD68 (Abcam), while 4′,6-diamidino-2-phenylindole (DAPI) (Southern Biotech, Bama, USA) was employed for nucleus staining. Furthermore, transverse sections derived from mid-regenerated nerves were stained using uranyl acetate and lead citrate, and then observed under a transmission electron microscope (TEM, HT7700, JEOL Ltd., Tokyo, Japan) with photographs captured across 10 random fields from each section. Quantification of regenerative axons was achieved using ImageJ software (https://imagej.nih.gov/ij/index. html). Additionally, a semi-automated software, MyelTracer, facilitated quantification of myelin g-ratio [29].

2.8. Muscle and motor endplate staining

The cross-sections of the gastrocnemius muscle (12 μm) were subjected to laminin (1:50, Abcam) staining to calculate the average cross-sectional area of muscle fibers. For the observation of motor endplates, longitudinal sections of the gastrocnemius (25 μm) were incubated with α-bungarotoxin (α-BGT) (1:600, Sigma) and DAPI for observation of motor endplates. The areas of muscle fibers were counted by ImageJ software.

2.9. RNA-seq analysis

Bridged segments between proximal and distal junctions were sampled thrice from each experimental groups (hBMSC-dECM, autograft, and sham groups) at day 1, 3, 7 and week 2, 3, 4, 8, 12. According to the manufacturer's protocol, the 72 ribonucleic acid (RNA) samples were extracted using Trizol (Life technologies, Carlsbad, CA, USA). RNA purity and integrity were tested by NanoDrop 2000 (Thermo Fisher, USA) and Agilent 2100 (Agilent Technologies, Santa Clara, CA, USA), respectively. Strand-specific RNA-seq libraries were constructed, and the samples were sequenced using the Illumina Novaseq 6000 sequencing platform (Gene Denovo, Guangzhou, China). All subsequent analyses were performed using clean reads. The raw sequence data generated within this study have been submitted to the Genome Sequence Archive in BIG Data Center (https://bigd.big.ac.cn), Beijing Institute of Genomics (BIG), Chinese Academy of Sciences, under the accession number CRA010000.

2.10. Bioinformatics analysis

The edgeR package (https://www.rproject.org/) was used to identify differentially expressed genes (DEGs). Based on the results of differential expression analysis, DEGs of significance were defined as having a false discovery rate (FDR) < 0.05 and $|\log_2 FC| > 1$. Correlation analysis was performed using the R method and quantified by the Pearson's correlation coefficient. Principal component analysis (PCA) was executed using the R package gmodels (https://www.rproject.org/). Venn diagrams were plotted utilizing the VennDiagram R package (https://bioinformatics.psb.ugent.be/webtools/Venn/). DEGs were mapped to Gene Ontology (GO) terms (https://www.geneontology. org/) and the number of genes per term was calculated. Pathway enrichment analysis was carried out with the Kyoto Encyclopedia of Genes and Genomes (KEGG) pathway serving as the unit. A hypergeometric test was conducted to calculate a P value in comparison with the background genes, with the calculated P value corrected using FDR≤0.05 as the threshold. Pathways that met this condition were defined as significantly enriched pathways within the DEGs. Cytoscape (https://www.cytoscape.org) was employed to analyze gene co-expression networks within diverse biological processes. Genes with $|\log_2 FC| > 2$ were considered as significantly expressed.

2.11. Quantitative real-time polymerase chain reaction (qRT-PCR)

Total RNA was reverse transcribed utilizing the PrimeScript RT Reagent Kit (TaKaRa Bio, China). To quantify gene expression, qRT-PCR was conducted with the TB Green Premix Ex Taq (TaKaRa) on a StepOnePlus RT-PCR system (Applied Biosystems, USA). The relative mRNA levels were determined using the comparative 2-ΔΔCt method and were standardized to GAPDH levels. Each experiment was carried out three times for accuracy. The primer sequences can be found in Table S1.

2.12. Statistical analysis

Quantitative data were expressed as mean ± standard deviation (SD). A one-way analysis of variance (ANOVA) was employed to compare the means of multiple independent groups. The Graph-Pad Prism 8.0 software (Graph-Pad Software Inc., La Jolla, CA, USA) was used for statistical analysis. A p-value < 0.05 was considered to indicate statistical significance.

3. Results

3.1. Characterization of hBMSC-dECM and cell-matrixed nerve grafts

Upon stimulation with 50 μg/mL ascorbic acid, hBMSCs displayed a marked increase in ECM secretion (Fig. 1A). Prior to decellularization, the cells exhibited a tightly packed arrangement under light microscopy (Fig. 1D). Following decellularization, a flat and viscous layer of dECM film exhibiting a reticulated structure on the base of the dish (Fig. 1E). Under the SEM, hBMSC-dECM showed a dense fibrous meshwork structure with spheres of varying magnitudes interspersed between the meshwork fibers, exhibiting a certain directionality (Fig. 1F). Immunochemical stains using antibodies against fibronectin (green), collagen I (red), collagen IV (red), and laminin (red) have spotlighted the presence of these four major ECM proteins, post decellularization treatments of cultured hBMSCs (Fig. 1G–I), suggesting the maintenance of bioactivity in the hBMSC-dECM. A gelatinous membrane-like dECM was rolled into 6–8 layers around a PLGA axis and then threaded into a chitosan conduit to construct the cell-matrixed nerve graft (Fig. 1B and C). Viewed under the SEM, the thick fluffy dECM was deposited on the PLGA (Fig. 1J and K) and the inner wall (Fig. 1L and M) of the conduit, demonstrating certain directionality spheres of different sizes distributed between the fibers.

3.2. Functional recoveries of sensory and motor nerves

At week 12 postoperatively, the results of gait analysis showed that the hBMSC-dECM group maintained a stable stance with a sizable footprint area and high foot contact intensity (Fig. 2B). This group possessed no significant variance in SFI as compared to the autograft
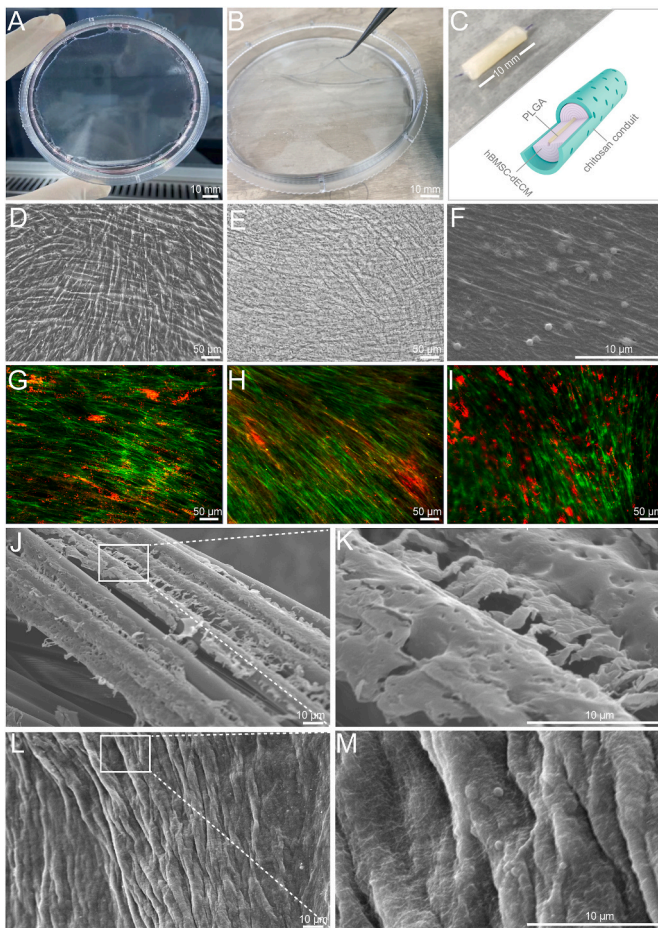
Fig. 1. Characterization of hBMSC-dECM and cell-matrixed nerve grafts. Appearance of pre-decellularized hBMSCs (A) and the hBMSC-dECM (B). Full view (top-left section of C) and schematic diagram (bottom-right section of C) of the cell-matrixed nerve graft. Light microscopic features of pre-decellularized hBMSCs (D), hBMSC-dECM (E), and scanning electron micrographs of hBMSC-dECM (F). Immunofluorescence micrographs of the hBMSC-dECM showing the co-expression of Fibronectin (green) + Collagen I (red) (G), Fibronectin (green) + Collagen IV (red) (H), and Fibronectin (green) + Laminin (red) (I). (J) Scanning electron micrographs showing the ultrastructure of cell-matrixed grafts with hBMSC-dECM wrapped around PLGA and the local high magnification image (K) as well as with hBMSC-dECM deposited on the conduit wall (L) and the local high magnification image (M).

group (Fig. 2C). The hBMSC-dECM and autograft group showcased similar paw withdrawal thresholds of 41.28 ± 14.85 g and 39.2 ± 15.32 g respectively, both significantly higher than the sham group at 19.55 ± 2.57 g (Fig. 2D). No significant disparity was observed in paw withdrawal latency between the hBMSC-dECM group, with a measurement of 16.3 ± 1.74 s, and the autograft group, at 15.36 ± 1.82 s (Fig. 2E). CMAPs in the hBMSC-dECM group achieved 71.85% of the sham group's comparable measurements, yet remained statistically indistinguishable from the autograft groups (Fig. 2F and G).

3.3. Observation of the regenerated nerve

The regenerating axon area in both the hBMSC-dECM and autograft groups did not show a significant difference, although it was comparatively lower than that in the sham group. HE staining of the hBMSC-dECM group demonstrated the organized arrangement of axons and myelin, dispersed in clusters (Fig. 3B and C). TEM further revealed the presence of numerous unmyelinated and myelinated nerve fibers. Remarkably, the myelinated axons in the hBMSC-dECM group were

enclosed by a distinct, thick, and electron-dense myelin sheath, although slightly thinner than that observed in the sham group (Fig. 3B). Myelinated nerve diameters of the regenerated nerves in the hBMSC-dECM, autograft, and sham groups were 2.6 ± 0.4, 2.95 ± 0.25, and 5.26 ± 1.23 μm, respectively (Fig. 3D). Nerve myelin thickness within the hBMSC-dECM, autograft and sham groups was 0.69 ± 0.03, 0.81 ± 0.13, and 1.94 ± 0.17 μm, respectively (Fig. 3E). G-ratio measurements in the hBMSC-dECM, autograft and sham groups were 0.64 ± 0.03, 0.65 ± 0.03, and 0.55 ± 0.03, respectively (Fig. 3F). The number of myelin layers in the hBMSC-dECM group, autograft group, and sham group were 45.29 ± 4.6, 51.43 ± 3.4, and 84.57 ± 12.9, respectively (Fig. 3B and G). We also showed the distribution of macrophages marked by CD68 (Fig. S1). Notably, there were no significant differences in these metrics between the hBMSC-dECM and autograft groups.

3.4. Target muscle correlation analysis

In the hBMSC-dECM, autograft, and sham groups, the cross-sectional areas of the muscle fibers were respectively 923.4 ± 98.85, 1131 ± 92.23, and 1606 ± 229.9 μm² (Fig. 4B and F). Statistical assessment showed no significant disparity between the hBMSC-dECM and autograft groups. Muscle wet weight ratios in these groups stood at 0.48 ± 0.22, 0.58 ± 0.16, and 0.88 ± 0.06 (Fig. 4C and E). There was no statistical difference between the hBMSC-dECM and autograft groups. The sham group presented predominantly mature-stage motor endplates, characterized by comparatively expansive butterfly-winged plaques and reticulated porous structures. The motor endplates in both hBMSC-dECM and autograft groups primarily exhibited elliptical plaques of smaller dimensions, indicating a state of intermediate maturation (Fig. 4B). Interestingly, the percentage of motor endplates in the hBMSC-dECM group that had reached the mature stage (47.6%) closely resembled that observed in the autograft groups (47.8%), revealing no substantial differences between them (Fig. 4G).

3.5. Hierarchical clustering and principal component analysis

We conducted hierarchical clustering (HCL) and PCA. The results of PCA analysis revealed distinct bifurcation of gene expression into two clusters within the hBMSC-dECM group. In this construct, the samples harvested on day 1 segregated into a unique category markedly different from others. Meanwhile, samples procured at the subsequent time points of day 3, 7, as well as week 2, 3, 4, 8, 12, shared similar changes (Fig. 5A). Within the autograft group, the gene expression was relatively uniform and broadly scattered, with day 1 clustered relatively into one group and week 12 showing a trend close to day 1 (Fig. 5B). The sham group exhibited a relatively focused gene expression, characterized by the day 1, week 8, and week 12 forming one cluster and day 3, 7 and week 2, 3, 4 an alternative cluster (Fig. 5C). Consequently, these contrasting patterns revealed unique characteristics for each PCA principal component. This also highlighted the overall variance in gene expression during regeneration across different intervention models, further substantiated by the gene distance matrix and HCL cluster analyses (Fig. 5D and E).

3.6. Differential gene expression

The temporal distribution of DEGs (compared with day 1) in the hBMSC-dECM, autograft and sham groups, demonstrated an escalation in the count of up-regulated genes over time, reaching a zenith at week 2 before stabilizing. Remarkably, the hBMSC-dECM group had the superior count of up-regulated genes at each time point (Fig. 5F). A comparison of the hBMSC-dECM group with the autograft highlighted a greater number of up-regulated and down-regulated genes in the former. The number of up-regulated genes peaked at week 2 in both groups and then showed a slow decline in the autograft group and remained relatively stable in the hBMSC-dECM group after 3 weeks (Fig. 5G). Venn
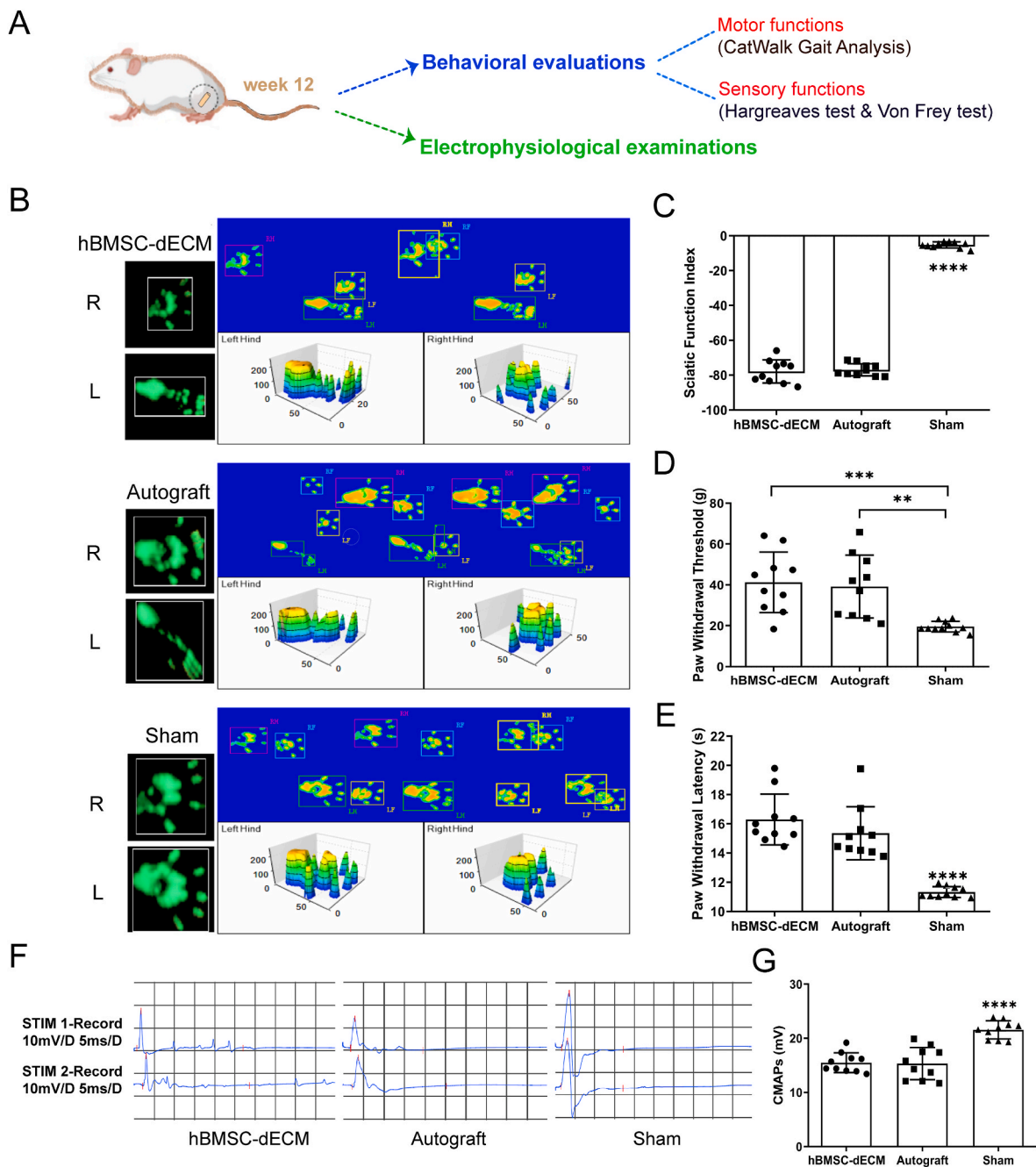
Fig. 2. Postoperative neurological function assessment at week 12. (A) Neurological function assessment protocol for each group. (B) Footprint results (top) and footprint 3D pattern map (bottom) for each group on the operated side (left hindfoot) and the healthy side (right hindfoot). (C) Comparison of sciatic nerve function index. (D) Von Frey method for testing paw withdrawal threshold. (E) Hargreaves method for testing paw withdrawal latency. CMAP waveforms (F) and intergroup comparison of the amplitude of CMAP at the proximal end (G). **p < 0.01, ***p < 0.001, ****p < 0.0001; one-way ANOVA; n = 10 animals/group.

analysis exposed variations in the number of distinctive and common DEGs across the three groups over different time points. At week 2, the peak in common DEGs was observed, which thereafter exhibited a gradual decrease (Fig. S2). DEGs in the hBMSC-dECM group and autograft group were divided into eight clusters following a heat map clustering analysis. Gene expression trends were discernible within these clusters, with noteworthy divergence in common genes between the hBMSC-dECM and autograft group (Fig. 5H and I).

3.7. GO and KEGG enrichment analysis

The top 10 GO terms identified by q-values in the hBMSC-dECM and

autograft groups at eight time points were combined and analyzed (including cellular components, biological processes, and molecular functions). Within the hBMSC-dECM group, significant enrichment of DEGs in "plasma membrane part" was observed consistently across all time points. In the initial 7 days, considerable DEG enrichment was seen in the "intrinsic component plasma membrane" and the "extracellular matrix", while there was enrichment at the "cell surface" at week 2. In terms of biological processes, a fluctuating pattern of DEG enrichment was displayed throughout the regeneration cycle, with intensified levels during in the initial and concluding stages, but a relative weakening in the intermediate phase. It was particularly notable during the first 3 days, with enrichments observed in areas of "development process",
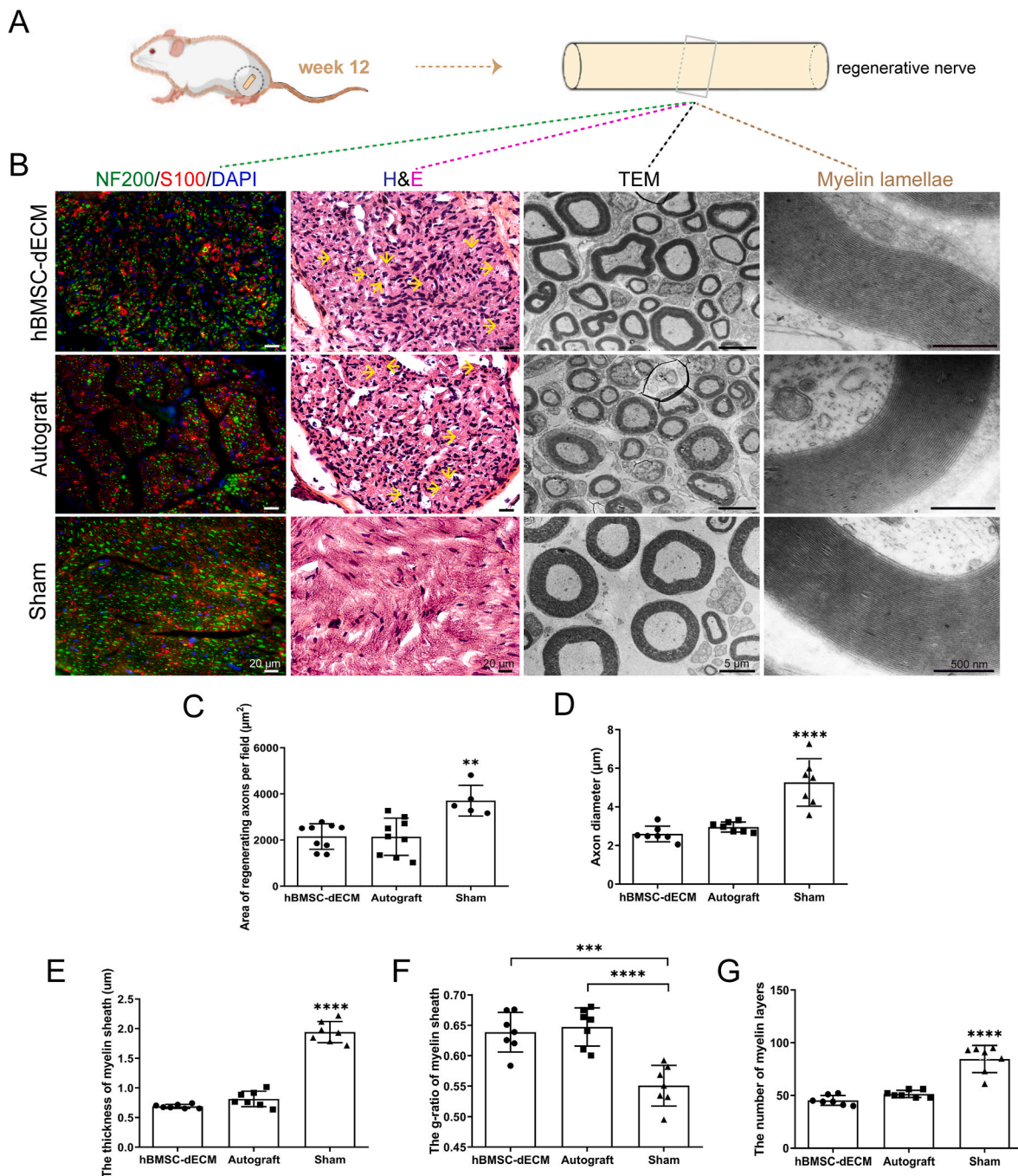
Fig. 3. Observation of regenerated axons and myelin sheaths in each group at week 12. (A) Morphological assessment protocol for regenerated sciatic nerves in each group. (B) Regenerated sciatic nerves co-labeled with anti-NF200 (green) and S100 (red) in each group (the first column); The images of HE staining of different groups (the second column) and regenerated nerve fibres are marked with yellow arrows; Transmission electron micrographs of regenerated nerves (the third column) and myelin laminae in each group (the fourth column). (C) Regenerated axon area (n = 9 animals/hBMSC-dECM & autograft; n = 5 animals/sham). (D) Regenerated axon diameter (n = 7 animals/group). (E) Myelin lamina thickness (n = 7 animals/group). (F) Myelinated nerve fiber G-ratio (n = 7 animals/group). (G) Myelin layers analysis (n = 7 animals/group). **p < 0.01, ***p < 0.001, ****p < 0.0001; one-way ANOVA.

"system development", "anatomical structure development", "regulation of multicellular organismal process", "regulation of response to stimulus", "cell adhesion", and "biological adhesion". For the molecular function, DEGs were significantly enriched in "protein binding" throughout all-time points (Fig. 6A).

In the autograft group, DEGs exhibited a striking enrichment in elements of the cellular component related to the extracellular matrix, specifically the "collagen-containing extracellular matrix", "plasma membrane part", and "extracellular region part", during the initial days post-operative. This propensity extended to the biological processes, where a strong early yet weakening later trend was noted, with DEGs favouring enrichment in pathways concerning "system development", "multicellular organism development", "development process", and "anatomical structure development" across all time points, with a marked emphasis on day 1. For the molecular function, DEGs were significantly enriched in "protein binding" at week 2 (Fig. 6B).

Biological functions are dictated by molecular interactions via upstream and downstream signals. By pooling the top 10 DEGs-enriched
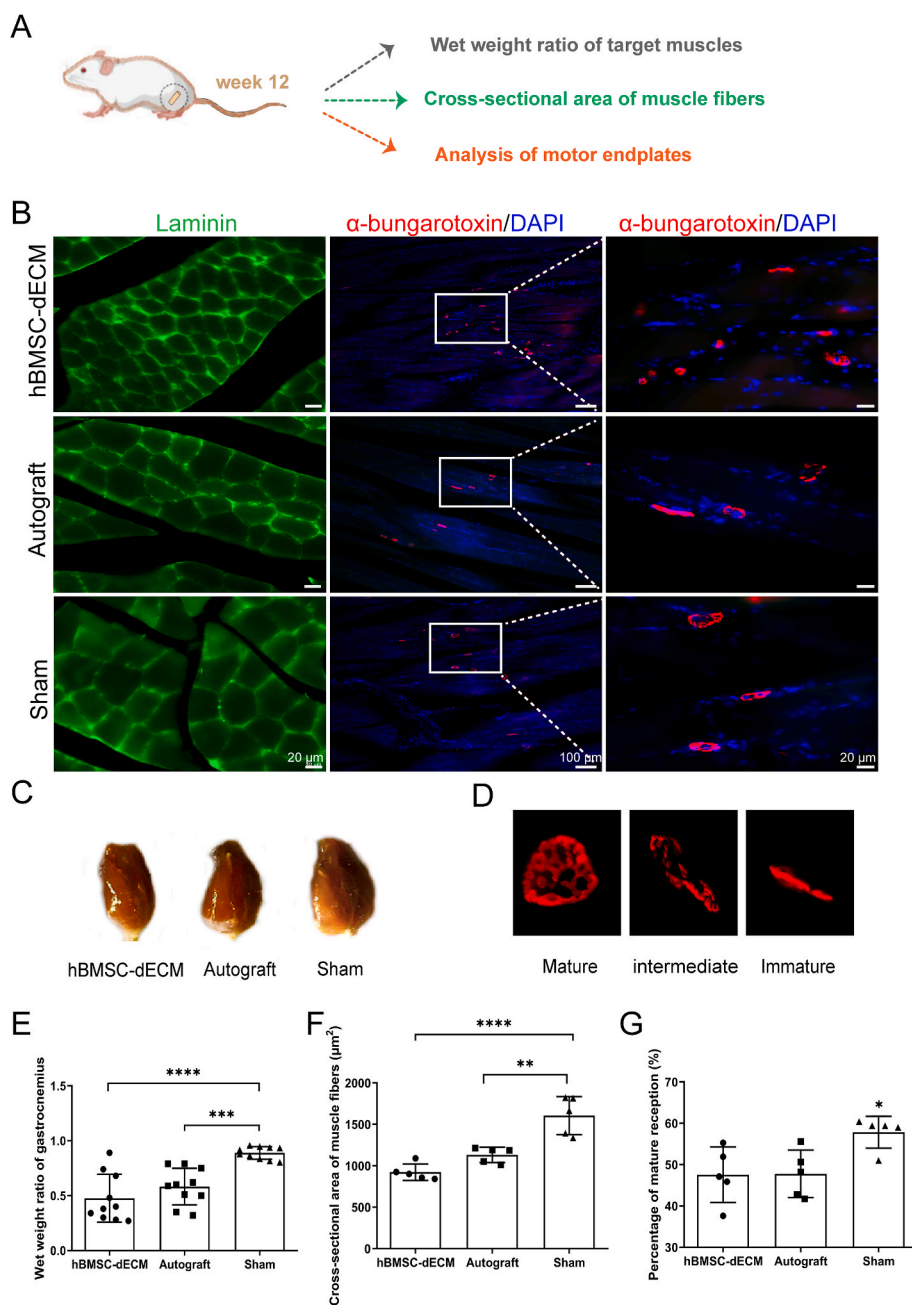
Fig. 4. Target muscle reinnervation in each group at week 12. (A) Functional recovery assessment protocol for target muscles in each group. (B) Gastrocnemius muscle fibers on the operated side stained with Laminin (green) and muscle fiber cross-sectional area (left column); motor endplates of the gastrocnemius muscle on the operated side co-stained with α-bungarotoxin (red) and DAPI (blue) (middle column); high magnification images of local motor endplates (right column). (C) Appearance of the gastrocnemius muscle on the operative side in each group. (D) Schematic diagram of motor endplate maturation. Motor endplates were divided into different stages: (1) mature with large, reticulated and porous structures; (2) intermediate (between the mature and immature stages); (3) immature with linear, non-porous structures. (E) Wet weight ratio of target muscles on the operative side in each group (n = 10 animals/group). (F) Cross-sectional area of gastrocnemius muscle fibers on the operative side in each group (n = 5 animals/group). (G) Motor endplate maturation in each group (n = 5 animals/group). *p < 0.05, **p < 0.01, ***p < 0.001 and ****p < 0.0001; one-way ANOVA.

pathways at each time point, a picture of different pathway enrichments and the significant trends in both groups gets painted. Particularly in the hBMSC-dECM group, the initial postoperative day witnessed the activation of "axon guidance", "focal adhesion", and "metabolic pathway". During the subsequent days, the "cell adhesion molecules", "cytokine-cytokine receptor interaction", and "P13K-Akt signaling pathway" were activated, registering a more pronounced enrichment compared to the autograft group (Fig. S3).

3.8. Interaction networks of axon and myelin-related genes

Specific attention was paid to the expression of DEGs intricately involved in axon growth and myelination in the formulation of a gene-gene regulatory network. Compared with the sham group, the DEGs at each time point of the hBMSC-dECM and autograft groups were combined and the changes of q values related to axon and myelin regeneration were calculated. The regulation of axonal regeneration, including

axon guidance and extension, initiated at day 1, followed by a gradual upregulated with enhanced enrichment in axon extension within 7 days to 2 weeks, and remained relatively stable with no significant changes within 2–4 weeks, in the hBMSC-dECM group. Axonal regeneration then escalated to a higher level and began an upward trend at week 4 that lasted until week 12. This phase saw the continuation of axon guidance and extension regulation, with a proportional increase in DEGs numbers. We observed marked regulation of Tnr, Atp1a3, Draxin, Gbx2, Shh and Robo 3 molecules at this stage (Fig. 7A and B). The autograft group had an axonal regeneration peak at day 7, characterized by significantly increased axon regulation and evident molecular regulation of Vax1, Slc30a3, Gbx2, Syt 4, and Lrp2. Following 7 days, the axonal regeneration was down-regulated, mildly resurrecting at week 3, followed by dampening at week 4 and sustaining low levels in subsequent stages (Fig. 7A and C).

In terms of axonal regeneration regulation, the hBMSC-dECM group exhibited a gradual increase in regulation, while the autograft group
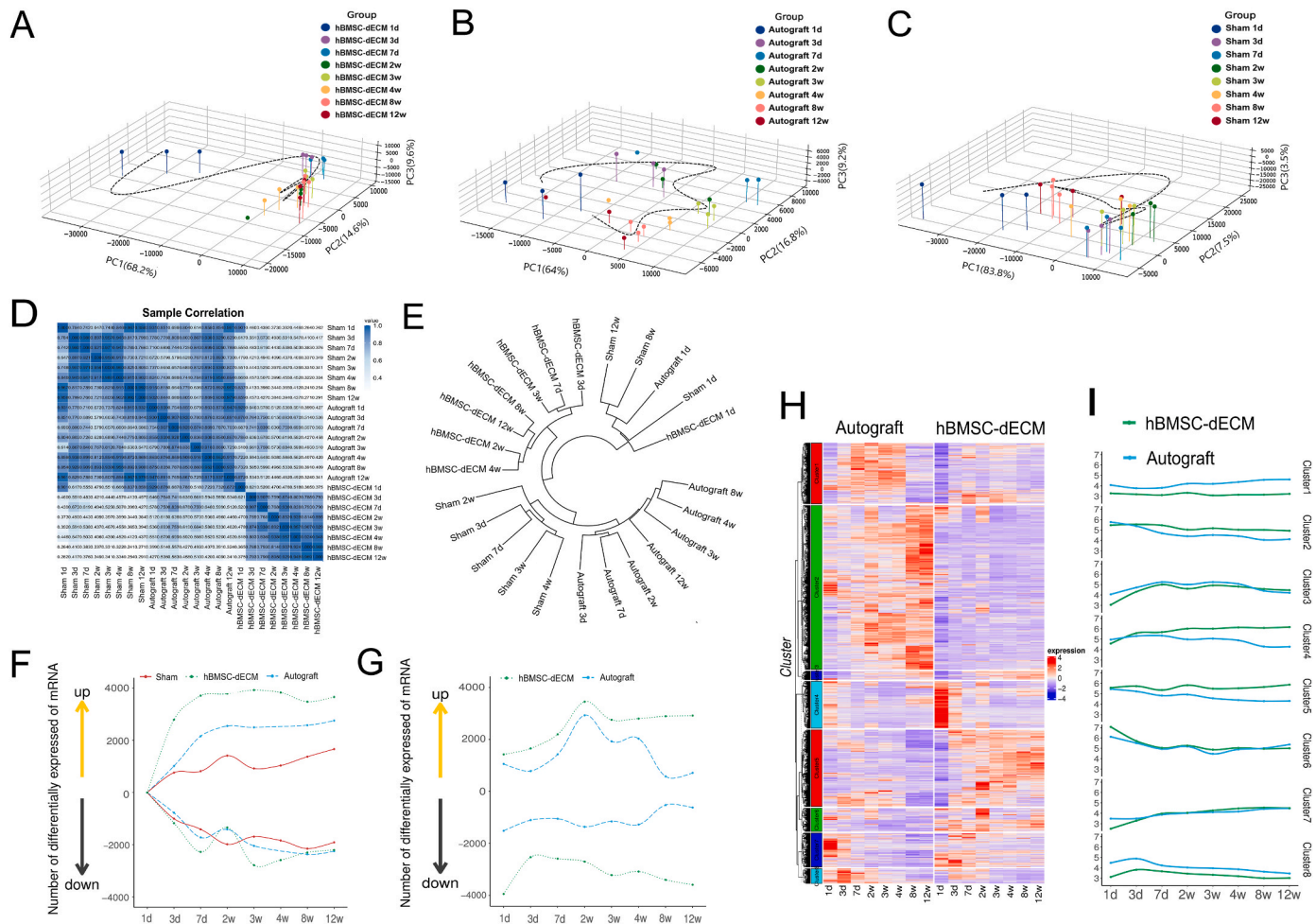
Fig. 5. Clustering characteristics and expression of differential genes in each group. (A–C) Principal component analysis of DEGs at different time points in each group. (D) Heat map of correlation between samples at different time points in each group. (E) Clustering tree of samples at different time points in each group. (F) The number of up- or down-regulated DEGs at different time points in each group (compared with that at day 1). (G) The number of up- or down-regulated DEGs at different time points in the hBMSC-dECM group and autograft group compared with the sham group. (H) Heat map of clustering of DEGs patterns at each time point in the hBMSC-dECM group and autograft group compared with the sham group. (I) Trends in DEGs variation at different time points in the hBMSC-dECM and autograft groups compared with the sham group.

demonstrated regulatory zeniths at day 7 and week 3, with remaining time points recording lower regulation levels.

In the hBMSC-dECM group, DEGs were significantly enriched for remyelination regulation at day 1. These DEGs included those integral to myelination, myelin sheath, and glial cell differentiation. Subsequently, this regulatory activity diminished, only to see a revitalized surge from day 7 to week 2 marked significant regulation of Schwann cell differentiation and glial cell activation, migration and differentiation, underscored by notable molecular regulation of Itgax, Hmga2, Sox11, Tp73, Mpz and Dlx 2. Remyelination regulation remained at a relatively stable and high level within 2–3 weeks and then declined again from week 3 to week 4. The regulation was gradually increased once again at week 4 and maintaining an elevated level until week 12, when the regulation of myelination, glial cell activation, differentiation and migration increased, with significant molecular regulation of Sox11, Trem2, Hmga2 and Ermn (Fig. 8A and B). In the autograft group, remyelination regulation peaked at day 3 after initiation, with a significant enrichment in the regulation of myelination and glial cell differentiation and significant molecular regulation of Sox11, Hmga2, Fgf 5, and Fa2h. Subsequently, remyelination regulation was gradually down-regulated and remained at a low level after 2 weeks (Fig. 8A and C).

Regarding myelin regeneration, the hBMSC-dECM group presented a

regulatory initial peak with following fluctuations and a later resurgence. The autograft group exhibited its zenith at day 3, with lower levels of regulation at the remaining time points.

3.9. Gene regulatory networks and data validation in the nerve regenerative microenvironment

Compared with the sham group, the DEGs at each time point of the hBMSC-dECM and autograft groups were combined and the q-values enriched for the ECM, vascularization, and immune regulation were calculated. Notably, the hBMSC-dECM group demonstrated significant ECM regulation at day 1. The key features included ECM component and ECM organization, as well as significant molecular regulation of Ero1a, Lingo 3, Thbs1, Mfap2 and Matn 4. A characteristic down-regulation over time was observed, with a marginal upregulation at week 3 and week 8, before descending and maintaining at low plateaus (Figs. S4A and B). The autograft group demonstrated a substantial regulatory alteration at day 1, incorporating significant modulation of ECM organization, collagen-containing ECM, and ECM binding. This regulation was accompanied by remarkable molecular regulation of Myf5, Thbs1, Elfn1, Col7a1, Bcan and Ntng1. Subsequently, ECM regulation was gradually downregulated and largely maintained at a low level, accompanied by a slight increase in regulation at week 4 (Figs. S4A and
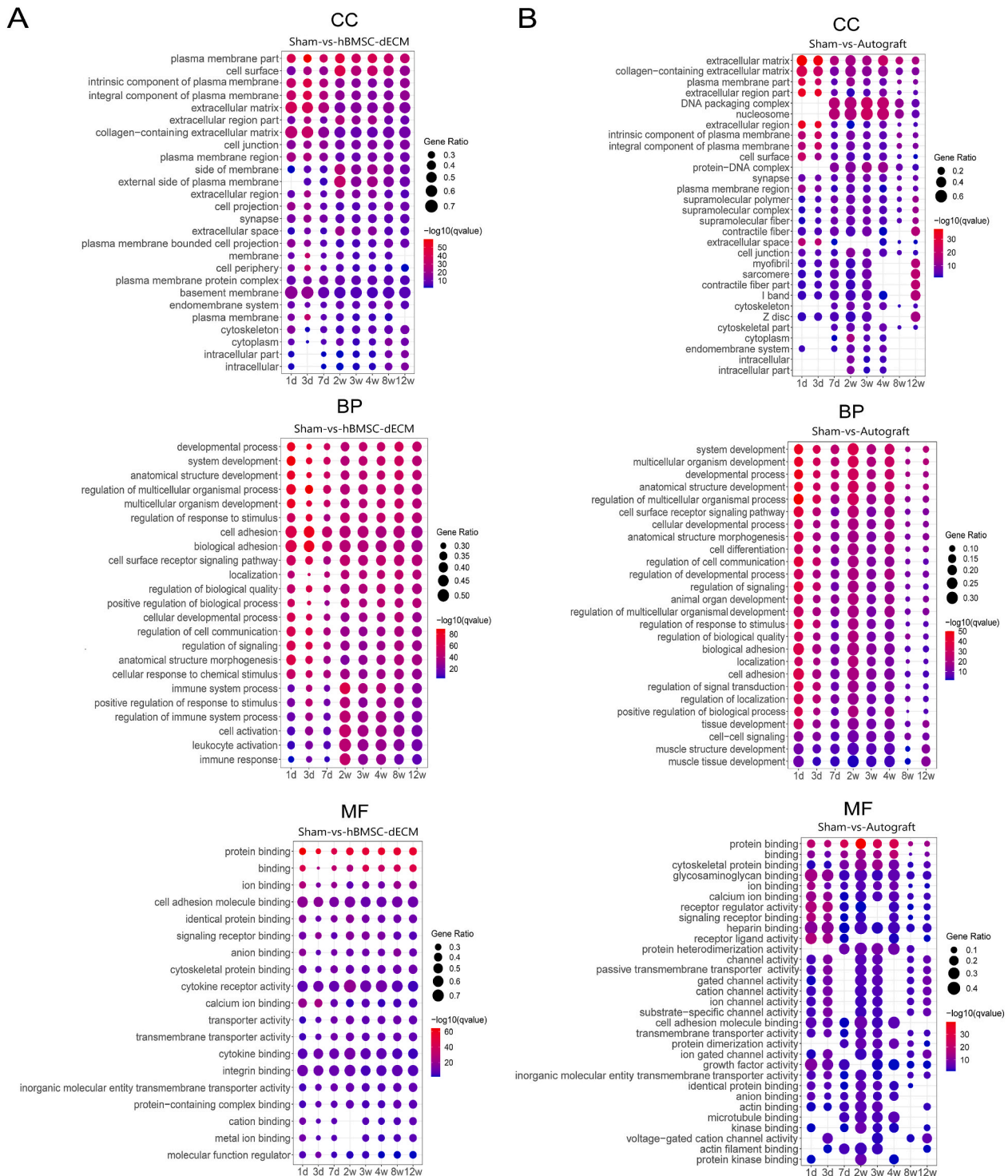
Fig. 6. Bubble plot for the top 10 enriched GO terms of DEGs (q-value). (A) Bubble plot for the top 10 enriched GO terms of DEGs at each time point in the hBMSC-dECM group compared with the sham group. (B) Bubble plot for the top 10 enriched GO terms of DEGs at each time point in the autograft group compared with the sham group.

C).

In terms of ECM regulation, both the hBMSC-dECM and autograft groups revealed a comparable regulatory trajectory, where primary-stage regulation was pronounced but progressively decreased in advanced stages.

The regulation of vascularization in the hBMSC-dECM group was particularly robust at day 1, characterized by significant enrichment in regulatory activities related to sprouting angiogenesis and vascular endothelial growth factor (VEGF) receptor signaling pathway. This was aided by significant molecular regulation involving Hmox1, Adra2c, Camp, Thbs1 and Chrm3. The active regulation progressively diminished from day 3 to day 7, and slightly increased thereafter from day 7 to week 2, leading to enhanced sprouting angiogenesis, before reducing again to maintain at low levels. From week 4–8, regulatory activity was marginally increased again, with an enhanced focus on positive regulation of angiogenesis and VEGF receptor signaling pathway, dwindling
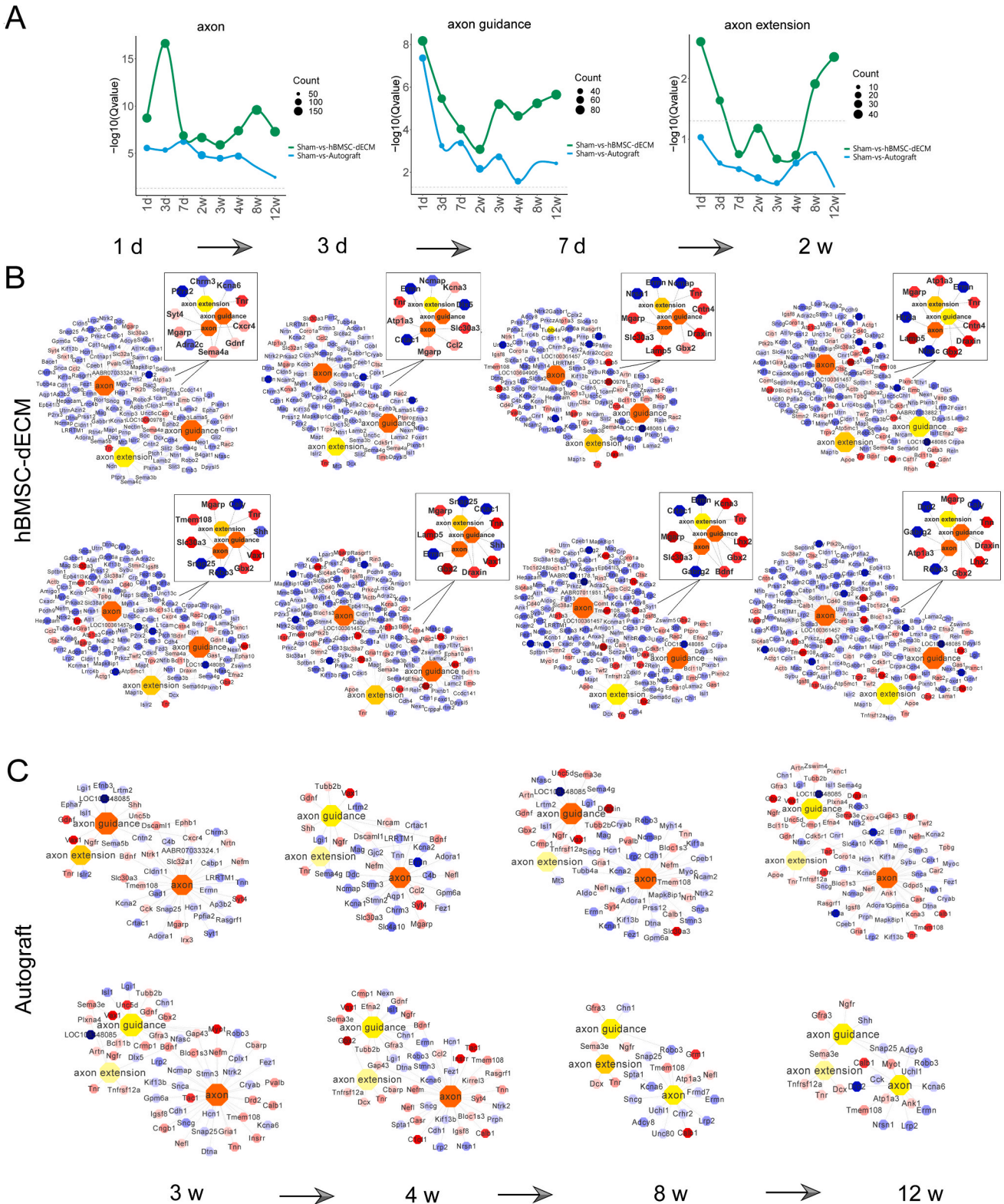
Fig. 7. Axonal regeneration-related molecular regulations in the hBMSC-dECM and autograft groups. (A) Trends in q-values of combined DEGs enriched for axons, axon guidance, and axon extension in the hBMSC-dECM and autograft groups compared with the sham group at each time point. (B) Expression and regulatory network of axonal regeneration-related genes in the hBMSC-dECM group. A partial display of key gene networks are marked with the black box. (C) Expression and regulatory network of axonal regeneration-related genes in the autograft group. A large circle represents a GO term and a small circle represents a gene. The connecting line indicates the pathway to which the gene belongs. Small circles are colored in red to indicate that the gene is upregulated at the given time point, and in blue to indicate that the gene is downregulated. Log$_2$FC is represented by the depth of shade. Large circles are colored to indicate the p-value of the pathway, while their sizes indicate the enrichment factor of the pathway (the number of DEGs divided by all genes in the GO term).
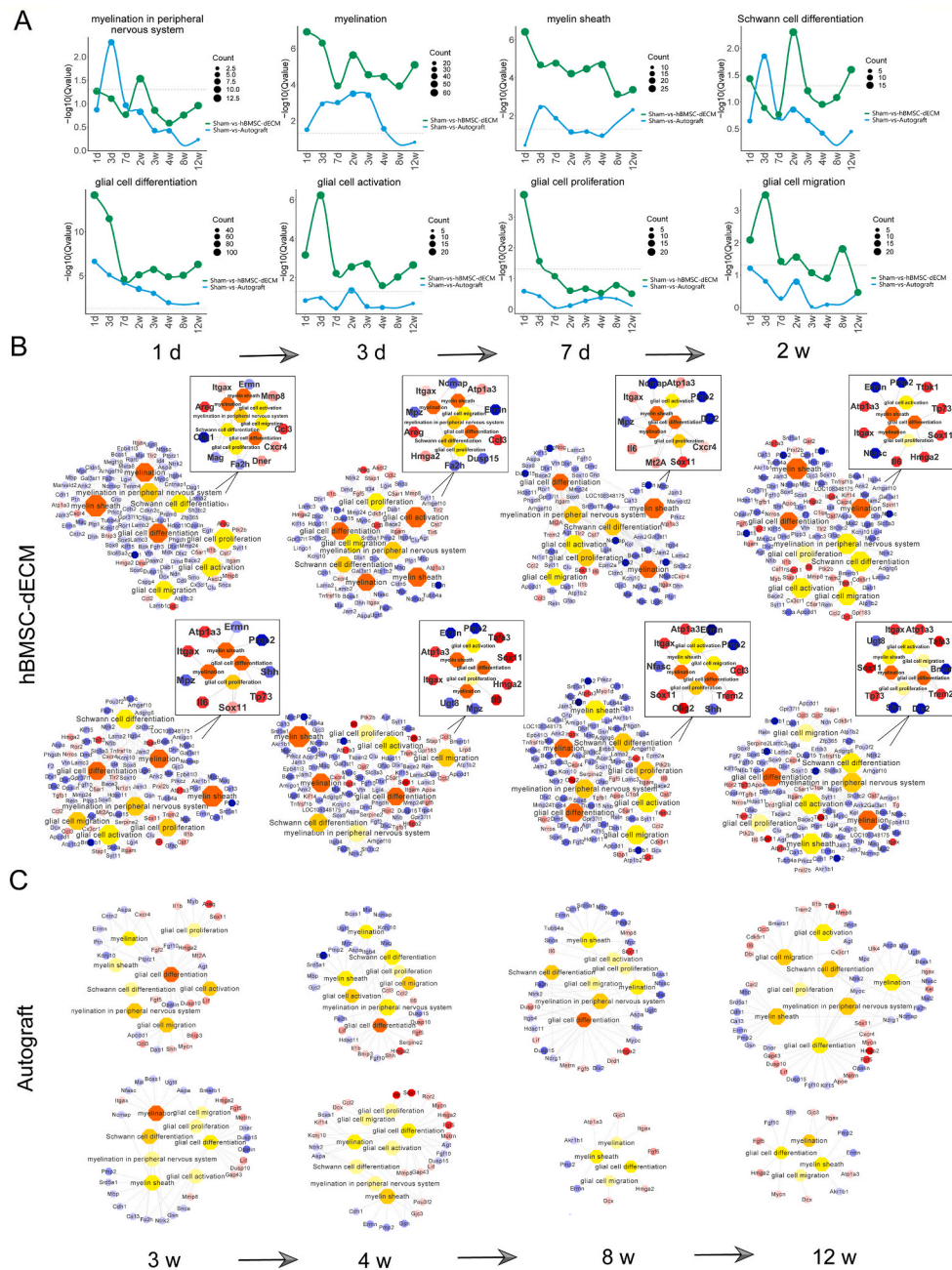
Fig. 8. Remyelination-related molecular regulations in the hBMSC-dECM and autograft groups. (A) Trends in q-values of combined DEGs enriched for myelination, myelin sheath, glial cell activation, migration and differentiation in the hBMSC-dECM and autograft groups compared with the sham group at each time point. (B) Expression and regulatory network of remyelination-related genes in the hBMSC-dECM group. A partial display of key gene networks are marked with the black box. (C) Expression and regulatory network of remyelination-related genes in the autograft group.

after 8 weeks (Figs. S5A and B). The autograft group demonstrated a comparable pattern of vascular regulation to that observed in the hBMSC-dECM group. Particularly rapid regulatory activitiesy were apparent on day 1, albeit less pronounced than in the hBMSC-dECM group, comprised of significant regulation of sprouting angiogenesis, VEGF receptor signaling pathway, positive regulation of angiogenesis and regulation of blood vessel diameter. The molecular regulation involved Adm 2, Adrb3, Hmox1, Camp and Hmga2. The pace of vascularization regulation moderation decreased steadily until day 7, followed by two smaller peaks of activity at week 2 and week 4. This period saw an enhanced regulation of positive regulation of angiogenesis and regulation of blood vessel diameter. Regulatory activities were maintained at low levels at the other time points (Figs. S5A and C).

During the regulation of vascularization, the hBMSC-dECM and autograft groups showed relatively similar regulation trends, both of which were significant in the early stage and then reduced to a lower level for fluctuating regulation.

Immunoregulation in the hBMSC-dECM group was slightly upregulated at day 3 and then declined, including neutrophil and lymphocyte activation, and T cell activation and differentiation. Immunoregulation was increased again and peaked at week 2, concomitant with an upswing in DEGs. At this stage, it was apparent that both the innate and acquired immunity were considerably invigorated, underscored by the pivotal role of several molecules including Pou2af1, Nkx 2-3, Xcl1, Foxp3 and Fgl2. A subsequent precipitous drop in immunoregulation ensued, stabilizing at a diminished level and eventually dwindling to baseline levels at week 12 (Figs. S6A and B, S7A and B). In the autograft group, the global immunoregulatory activity appeared minimally triggered, marked only by a slight elevation at week 2. Specifically, a slight increase of innate immunity-associated neutrophil activation occurred, bolstered by enhanced regulation of molecules such as Exosc6, Itgb2 and Pck1. Concurrently, a slight upregulation in acquired immunity-related T cell activation was observed, coupled with the accelerated regulation of molecules including Xcl1, Il6, Exosc6, Rps 6 and Fgl2 (Figs. S6A and

C, S7A and C).

In terms of immune regulation, the hBMSC-dECM group attained an apex of regulation at week 2, which ebbing thereafter and ultimately restored to baseline levels. The autograft group demonstrated a slight increase in immunoregulation at week 2, with no significant activation overall.

To corroborate the fidelity of our sequencing data, we instigated the qRT-PCR targeting the expression levels of six key genes implicated in the regulatory process of nerve regeneration, including Gbx2, Hmox1, Col7a1, Shh, Itgax, and Ccl2. Interestingly, our results demonstrated a strong correlation in mRNA expression across RNA-seq analysis and qRT-PCR analyses for all selected genes (Fig. S8). This consistent alignment affirms the meticulosity and trustworthiness of our findings.

4. Discussion

The goal of peripheral nerve repair is to minimize recovery time and maximize function rehabilitation. As a biological material, the advantages of the ECM are that it provides an excellent microenvironment for cells, directs them towards differentiation specifically or maintenance of different phenotypes, and provides a specific physical structure for tissue and organ regeneration. Moreover, abundant biochemical signals in the ECM act as regulatory factors to regulate host cell differentiation, proliferation, morphogenesis, signal transduction and tissue remodeling [30,31]. Although dECM derived from tissues have biochemical and physical factors that support the growth of cells and tissues [32], the consistent provision of quality donor tissue constitutes a prominent constraint. Recognized challenges linked to tissue-derived dECM comprise pathogen transmission, uncontrolled degradation, and high manufacturing costs [33–35]. Nevertheless, the cell-based dECM with more advantages can be used to engineer scaffolds with different three-dimensional shapes and structures and other additional features to produce biomimetic tissue structures, and can be customized by selecting specific cells from a particular tissue or individual to overcome the limitations of homo- or xenotransplantation.

In this study, we ingeniously employed hBMSC-derived dECM around biodegradable scaffolds to create a novel and advanced cell-matrixed nerve graft. This remarkable approach not only establishes a conducive pathway for the growth of neuronal cells but also offers precise guidance and orientation to ensure their proper development. The dECM and cell-matrixed nerve grafts were characterized by immunohistochemical staining and scanning electron microscopy. These components play a key role in maintaining the structural stiffness and elasticity of the material, providing the necessary mechanical properties and fine structural stability for the dECM [14]. The cell-matrixed nerve grafts developed in this study boasts excellent biocompatibility, biodegradability, coupled with a lack of any marked cytotoxicity [25]. Key features include their superior stereo-conformation and biological guidance performance, making them an ideal candidate for further exploration in the field of nerve regeneration.

To investigate the in vivo performance of the nerve graft, a 10-mm defect of the sciatic nerve of rat was bridged using the constructed cell-matrixed nerve graft. Behavioral, electrophysiological, and morphological parameters were contrasted between the hBMSC-dECM and autograft groups at week 12. The results revealed that the cell-matrixed nerve grafts exhibit a similar effect on nerve regeneration and corresponding functional recovery as autograft. This supportive effect may be associated with the dECM's capacity to supply substrates and conformations favorable to cell adhesion, growth, migration, and proliferation [36,37]. Immunostaining analysis revealed that the regeneration of axons in the hBMSC-dECM group exhibited a striking similarity to that observed in the autograft group. The results from the transmission electron microscopy and analysis of regenerated nerve fibers provide compelling evidence that the hBMSC-dECM modified scaffolds play a beneficial role in facilitating the formation of myelin sheaths.

Reinnervation of the target organ is an important indicator of the recovery of nerve function [38,39]. The wave amplitude of CMAPs is proportional to the number of nerve fibers reinnervating the target muscle. The test showed higher CMAPs wave amplitude in the hBMSC-dECM group and the degree of recovery was close to that of the autograft group. The gastrocnemius wet weight ratio and gastrocnemius motor endplates confirmed that the hBMSC-dECM group improved target organ reinnervation after sciatic nerve regeneration. Taken together, functional and histological investigations imply that the cell-matrixed nerve grafts foster the development of regenerative microenvironments that are conducive to axon growth.

To analyze the molecular regulatory patterns of cell-matrixed nerve grafts and autologous nerve grafts for the repair of peripheral nerve defects, we used GO functional enrichment analysis to annotate all DEGs in the bridging segment of the sciatic nerve in a hierarchical manner based on biological processes, cellular components, and molecular functions. Interestingly, an ecological diversity of biological processes was observed postoperatively at various time points within groups, underscored by a prominent enrichment of development-related processes at day 1 and day 3. This highlights the close association between regeneration and development. The regulation of stimulus response was also significantly enriched at day 1 and day 3. When the body is subjected to stimulus such as mechanical injury, it is inevitably accompanied by an inflammatory response, including the activation of neutrophils, macrophages, and lymphocytes, which are also enriched during the early stage of regeneration. The results are consistent with previous studies on the critical regulation of peripheral nerve regeneration by neuroimmune pathways [40]. In the hBMSC-dECM group, the enriched pathways, namely "axon guidance", "focal adhesion" [41], and "P13K-Akt signaling pathway" [42] were activated on day 1 to day 3, indicating that the cell-matrixed nerve grafts effectively activated axonal signaling and metabolic pathways at an early stage, and showed nerve regeneration results similar to those of autograft by regulating cell survival and adhesion as well as growth factor activity.

We also employed pathway enrichment analysis and gene co-expression network analysis. Given the critical role of axonal growth and myelin regeneration in peripheral nerve regeneration, we delved into the intricate regulatory mechanisms governing the genes implicated in these processes. The expression of gastrulation brain homeobox 2 (Gbx2) exhibited an upregulation at day 3 and remained consistently elevated for up to week 3. Previous studies demonstrated the pivotal involvement of Gbx2 in the precise regulation of axonal guidance in the thalamocortex, thus highlighting its crucial role in nervous system development [43]. Tenascin R (Tnr) exhibited sustained and robust expression in the hBMSC-dECM group as early as day 1. Tnr serves as a key facilitator of cell attachment and guides the growth of axons, thus assuming a critical role in the broader context of nerve regeneration [44]. ATPase Na+/K+ transporting subunit alpha 3 (Atp1a3), a critical protein involved in the maintenance of electrochemical gradients across cell membranes [45], exhibited significant upregulation in the regulation of both axonal and myelin regeneration in both groups. These findings strongly support the notion that cell-matrixed nerve grafts offer a significantly effective means to foster the growth of axons.

It is extremely significant to consider the major microenvironmental cues in the course of peripheral nerve regeneration when we design and fabricate functionally tissue-engineered nerve grafts. Thus, we undertook an extensive analysis of the immune cues present in these grafts. Our findings revealed a noteworthy early modulation in the hBMSC-dECM group compared to the autograft group. This modulation included activation of neutrophils, as well as differentiation and activation of T cells. Furthermore, the immune response modulation increased significantly, reaching its peak at week 2, accompanied by enhanced B cell and T helper type 1 cell modulation. These observations suggest that the biomaterials used induce a distinct foreign body response that differs from the response triggered by autologous nerves. However, we observed no substantial difference in macrophage

distribution between the hBMSC-dECM and autograft groups at week 12 (Fig. S1). This suggests that the inflammation had subsided in both groups during the later stages of transplantation. These results are consistent with the previous proteomic data obtained by another research group in our team. They discovered that nerve grafts modified with BMSC-ECM elicited significantly lower immune responses compared to grafts modified with ECM derived from other cellular sources such as Schwann cells, fibroblasts, and SKP-SCs, as well as acellular nerves [46]. Angiogenesis is an important process in peripheral nerve regeneration as it provides nutritional support and transports neurotrophic factors, proteins, and oxygen to the site of injury. Great efforts have been made to develop scaffolds based on pro-angiogenic nanomaterials, and porous formations in various polymeric scaffolds have been used to mimic ECM-like microenvironments in vitro [47–49]. In this research, we have focussed on the use of dECM, derived from natural cells, which have maintained the three-dimensional conformation of the extracellular matrix across scales from macro to micro, inclusive of nanoscale microenvironments. These matrices exhibit enhanced affinity towards various cells and can thereby stimulate key biological behaviors such as cell adhesion, migration, proliferation, and differentiation, thus underscoring their potential for diverse biological applications. The unique conformational characteristics of these decellularized matrices greatly enable them to act as efficient participants in the vasoregulatory processes, particularly in the early stage. Their intrinsic capability to exploit intraneural vascularization instigates potent therapeutic interventions, testifying the supreme potential in triggering potent therapeutic effects.

Finally, a comprehensive visual aid that encapsulates all the data and analyses was conducted (Fig. 9). It was able to showcase the unique biological processes, cellular components, and molecular functions of the hBMSC-dECM group at each stage of development. Moreover, we have identified distinct molecular regeneration patterns, which are critical for successful peripheral nerve regeneration. Our findings demonstrate that the cell-matrixed nerve grafts play a significant role in regulating axonal regeneration, remyelination, ECM, vascularization, and immune response over time. The regulation of ECM and vascularization was more similar, with a large number of molecular regulatory changes at the beginning of both. The regulation of the immune response reached its peak at week 2 and subsequently declined gradually to normal levels. Both the hBMSC-dECM and autograft groups initiated regenerative repair with ECM guidance and protection, particularly in the early stages of nerve regeneration. However, in the hBMSC-dECM group, nerve regeneration experienced more intense molecular regulation from inception. This group exhibited a more potent molecular regulation of nerve regeneration that began with vascularization and remyelination processes, followed by axonal processes and the upregulation of the immune response. Myelination and axonal regulation continued to interact in an orderly and synergistic manner, resulting in sustained and sufficient nerve regeneration. In contrast, the autograft group exhibited relatively smooth molecular regulation of nerve regeneration owing to its "innate advantage". It was initiated with vascular processes, followed by significant regulation of myelin and axonal processes, and a mild upregulation of the immune response. Multiple functions quickly returned to normal more after nerve regeneration in this group. However, several issues need to be addressed before BMSCs can be used for nerve injury treatments in clinical practice. For instance, the quantity and quality of BMSCs tend to decrease with donor age. Therefore, a normative strategy for quantitative comparison of the therapeutic function of different extracellular matrices remains to be explored. Achieving optimal temporal application of
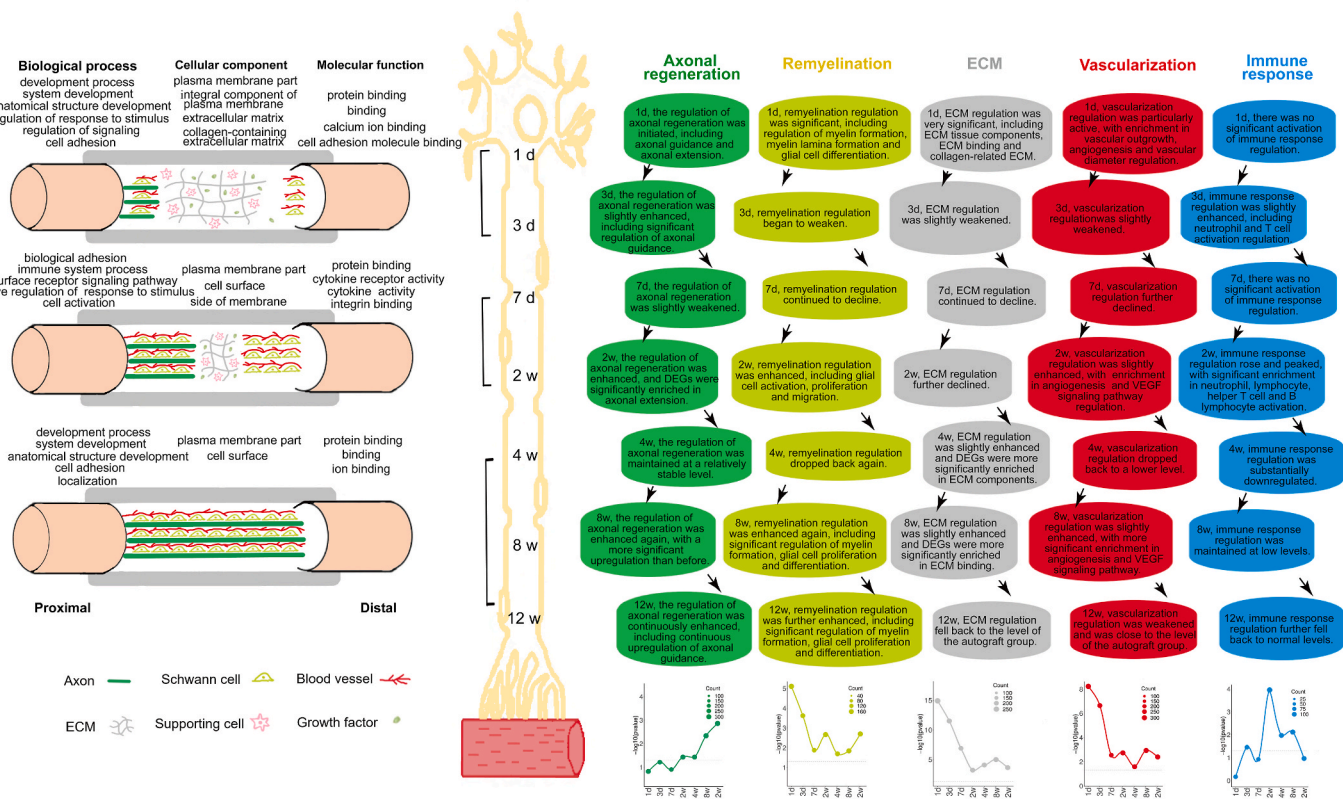
Fig. 9. Molecular mechanisms underlying the cell-matrixed nerve grafts for repair of peripheral nerve defects. Bioinformatics analysis shows the top 10 enriched GO terms of DEGs (q-values) at three different transcriptional stages (left part) in the hBMSC-dECM group from day 1 to week 12 postoperatively, including biological processes, cellular components, and molecular functions of each transcriptional stage, as well as a schematic diagram of the morphological changes of the injured sciatic nerve undergoing repair by the cell-matrixed nerve graft. Trends in the molecular regulation of the hBMSC-dECM group in terms of axonal regeneration, remyelination, ECM, vascularization, and immune response over time (day 1, 3, 7 and week 2, 4, 8, 12) and overall molecular regeneration patterns (right part).

dECM for therapeutic purposes involves various critical aspects, such as cell culture conditions, dECM extraction methods, yield, and purity.

5. Conclusion

The research demonstrated that hBMSC-dECM-modified nerve grafts possess remarkable repair properties, offering a favorable microenvironment for peripheral nerve regeneration. Moreover, the exceptional biochemical and structural components present in hBMSC-dECM play vital roles in facilitating initial cell adhesion and guidance, as well as exerting spatio-temporal control over the microenvironment to stimulate continuous cellular responses fostering nerve regeneration. Moving forward, our objective is to develop flexible and personalized dECM-modified nerve grafts by utilizing patient-derived BMSCs in conjunction with scaffolds precisely tailored to the target tissue. This innovative approach holds great promise for the regenerative medicine, paving the way for the groundbreaking advancements in the near future.

Data availability

Data will be made available on request. The raw sequencing data from this study have been deposited in the Genome Sequence Archive in BIG Data Center (https://bigd.big.ac.cn), Beijing Institute of Genomics (BIG), Chinese Academy of Sciences, under the accession number CRA010000.

Ethics approval and consent to participate

All experimental procedures followed the Guide for the Care and Use of Laboratory Animals issued by the US National Research Council and approved by the Laboratory Animal Management Committee of Jiangsu Province, China (approval no: S20210309-009).

CRediT authorship contribution statement

Shanshan Wang: Investigation, Methodology, Data curation, Writing – original draft, Writing – review & editing. **Hongkui Wang:** Methodology, Investigation, Writing – review & editing. **Panjian Lu:** Methodology, Investigation. **Leilei Gong:** Investigation. **Xiaosong Gu:** Conceptualization, Methodology, Supervision, Funding acquisition. **Meiyuan Li:** Conceptualization, Investigation, Data curation, Supervision, Writing – review & editing, Funding acquisition.

Declaration of competing interest

The authors declare that they have no known competing financial interests or personal relationships that could have appeared to influence the work reported in this paper.

Acknowledgments

Appendix A. Supplementary data

Supplementary data to this article can be found online at https://doi.org/10.1016/j.bioactmat.2023.09.002.

References

[1] D.W. Hewson, N.M. Bedforth, J.G. Hardman, Peripheral nerve injury arising in anaesthesia practice, Anaesthesia 73 (Suppl 1) (2018) 51–60, https://doi.org/10.1111/anae.14140.

[2] P. Klimovich, K. Rubina, V. Sysoeva, et al., New frontiers in peripheral nerve regeneration: concerns and remedies, Int. J. Mol. Sci. 22 (24) (2021), https://doi.org/10.3390/ijms222413380.

[3] K.L. Colen, M. Choi, D.T.W. Chiu, Nerve grafts and conduits, Plast. Reconstr. Surg. 124 (6 Suppl) (2009) e386–e394, https://doi.org/10.1097/PRS.0b013e3181bf8430.

[4] Z. Huang, R. Powell, J.B. Phillips, et al., Perspective on Schwann cells derived from induced pluripotent stem cells in peripheral nerve tissue engineering, Cells 9 (11) (2020) 2497, https://doi.org/10.3390/cells9112497 (11) (2020).

[5] M. Jahromi, S. Razavi, A. Bakhtiari, The advances in nerve tissue engineering: from fabrication of nerve conduit to in vivo nerve regeneration assays, J. Tissue Eng. Regen. Med. 13 (11) (2019) 2077–2100, https://doi.org/10.1002/term.2945.

[6] C. Phamornnak, B. Han, B.F. Spencer, et al., Instructive electroactive electrospun silk fibroin-based biomaterials for peripheral nerve tissue engineering, Biomater. Adv. 141 (2022), 213094, https://doi.org/10.1016/j.bioadv.2022.213094.

[7] S. Vijayavenkataraman, Nerve guide conduits for peripheral nerve injury repair: a review on design, materials and fabrication methods, Acta Biomater. 106 (2020) 54–69, https://doi.org/10.1016/j.actbio.2020.02.003.

[8] X. Gu, Biodegradable materials and the tissue engineering of nerves, Engineering 7 (12) (2021) 1700–1703, https://doi.org/10.1016/j.eng.2021.10.011.

[9] X. Gu, Recent progress in biomaterials-tissue engineering, Engineering 13 (6) (2022) 1, https://doi.org/10.1016/j.eng.2022.04.005.

[10] U. Arif, S. Haider, A. Haider, et al., Biocompatible polymers and their potential biomedical applications: a review, Curr. Pharm. Des. 25 (34) (2019) 3608–3619, https://doi.org/10.2174/1381612825999191011105148.

[11] P. Lu, G. Wang, T. Qian, et al., The balanced microenvironment regulated by the degradants of appropriate PLGA scaffolds and chitosan conduit promotes peripheral nerve regeneration, Mater. Today Bio. 12 (2021), 100158, https://doi.org/10.1016/j.mtbio.2021.100158.

[12] P. Deng, F. Chen, H. Zhang, et al., Multifunctional double-layer composite hydrogel conduit based on chitosan for peripheral nerve repairing, Adv. Healthcare Mater. 11 (13) (2022), e2200115, https://doi.org/10.1002/adhm.202200115.

[13] M. Brown, J. Li, C. Moraes, et al., Decellularized extracellular matrix: new promising and challenging biomaterials for regenerative medicine, Biomaterials 289 (2022), 121786, https://doi.org/10.1016/j.biomaterials.2022.121786.

[14] A.D. Theocharis, S.S. Skandalis, C. Gialeli, et al., Extracellular matrix structure, Adv. Drug Deliv. Rev. 97 (2016) 4–27, https://doi.org/10.1016/j.addr.2015.11.001.

[15] N.K. Karamanos, A.D. Theocharis, Z. Piperigkou, et al., A guide to the composition and functions of the extracellular matrix, FEBS J. 288 (24) (2021) 6850–6912, https://doi.org/10.1111/febs.15776.

[16] A. Sainio, H. Järveläinen, Extracellular matrix-cell interactions: focus on therapeutic applications, Cell. Signal. 66 (2020), 109487, https://doi.org/10.1016/j.cellsig.2019.109487.

[17] H. Xing, H. Lee, L. Luo, et al., Extracellular matrix-derived biomaterials in engineering cell function, Biotechnol. Adv. 42 (2020), 107421, https://doi.org/10.1016/j.biotechadv.2019.107421.

[18] X. Zhang, X. Chen, H. Hong, et al., Decellularized extracellular matrix scaffolds: recent trends and emerging strategies in tissue engineering, Bioact. Mater. 10 (2022) 15–31, https://doi.org/10.1016/j.bioactmat.2021.09.014.

[19] Y. Guan, B. Yang, W. Xu, et al., Cell-derived extracellular matrix materials for tissue engineering, Tissue Eng., Part B 28 (5) (2022) 1007–1021, https://doi.org/10.1089/ten.TEB.2021.0147.

[20] H. Lu, T. Hoshiba, N. Kawazoe, et al., Cultured cell-derived extracellular matrix scaffolds for tissue engineering, Biomaterials 32 (36) (2011) 9658–9666, https://doi.org/10.1016/j.biomaterials.2011.08.091.

[21] F. He, M. Pei, Extracellular matrix enhances differentiation of adipose stem cells from infrapatellar fat pad toward chondrogenesis, J. Tissue Eng. Regen. Med. 7 (1) (2013) 73–84, https://doi.org/10.1002/term.505.

[22] M. Pei, F. He, Extracellular matrix deposited by synovium-derived stem cells delays replicative senescent chondrocyte dedifferentiation and enhances redifferentiation, J. Cell. Physiol. 227 (5) (2012) 2163–2174, https://doi.org/10.1002/jcp.22950.

[23] O.L. Abbas, O. Özatik, Z.B. Gönen, et al., Bone marrow mesenchymal stem cell transplantation enhances nerve regeneration in a rat model of hindlimb replantation, Plast. Reconstr. Surg. 143 (4) (2019) 758e–768e, https://doi.org/10.1097/prs.0000000000005412.

[24] L. Fan, C. Liu, X. Chen, et al., Exosomes-Loaded electroconductive hydrogel synergistically promotes tissue repair after spinal cord injury via immunoregulation and enhancement of myelinated axon growth, Adv. Sci. 9 (13) (2022), e2105586, https://doi.org/10.1002/advs.202105586.

[25] C. Xue, H. Ren, H. Zhu, et al., Bone marrow mesenchymal stem cell-derived acellular matrix-coated chitosan/silk scaffolds for neural tissue regeneration, J. Mater. Chem. B 5 (6) (2017) 1246–1257, https://doi.org/10.1039/c6tb02959k.

[26] R. Deumens, R.J. Jaken, M.A. Marcus, et al., The CatWalk gait analysis in assessment of both dynamic and static gait changes after adult rat sciatic nerve resection, J. Neurosci. Methods 164 (1) (2007) 120–130, https://doi.org/10.1016/j.jneumeth.2007.04.009.

[27] Q. Zhu, Y. Sun, L. Mao, et al., Antinociceptive effects of sinomenine in a rat model of postoperative pain, Br. J. Pharmacol. 173 (10) (2016) 1693–1702, https://doi.org/10.1111/bph.13470.

[28] C.S. Qiu, L.L. Wyhe, M. Sasaki, et al., Antinociceptive effects of MSVIII-19, a functional antagonist of the GluK1 kainate receptor, Pain 152 (5) (2011) 1052–1060, https://doi.org/10.1016/j.pain.2011.01.018.

[29] T. Kaiser, H.M. Allen, O. Kwon, et al., MyelTracer: a semi-automated software for myelin g-ratio quantification, eNeuro 8 (4) (2021), https://doi.org/10.1523/eneuro.0558-20.2021.

[30] C. Bonnans, J. Chou, Z. Werb, Remodelling the extracellular matrix in development and disease, Nat. Rev. Mol. Cell Biol. 15 (12) (2014) 786–801, https://doi.org/10.1038/nrm3904.

[31] Y. Chen, X. Dong, M. Shafiq, et al., Recent advancements on three-dimensional electrospun nanofiber scaffolds for tissue engineering, Adv. Fiber Mater. 4 (2022) 959–986, https://doi.org/10.1007/s42765-022-00170-7.

[32] R. Deng, Z. Luo, Z. Rao, et al., Decellularized extracellular matrix containing electrospun fibers for nerve regeneration:A comparison between core–shell structured and preblended composites, Adv. Fiber Mater. 4 (2022) 503–519, https://doi.org/10.1007/s42765-021-00124-5.

[33] J. Chato-Astrain, C. Philips, F. Campos, et al., Detergent-based decellularized peripheral nerve allografts: an in vivo preclinical study in the rat sciatic nerve injury model, J. Tissue Eng. Regen. Med. 14 (6) (2020) 789–806, https://doi.org/10.1002/term.3043.

[34] E. Contreras, S. Traserra, S. Bolívar, et al., Repair of long peripheral nerve defects in sheep: a translational model for nerve regeneration, Int. J. Mol. Sci. 24 (2) (2023), https://doi.org/10.3390/ijms24021333.

[35] D. García-García Ó, M. El Soury, F. Campos, et al., Comprehensive ex vivo and in vivo preclinical evaluation of novel chemo enzymatic decellularized peripheral nerve allografts, Front. Bioeng. Biotechnol. 11 (2023), 1162684, https://doi.org/10.3389/fbioe.2023.1162684.

[36] Z.C. Chan, M.J. Oentaryo, C.W. Lee, MMP-mediated modulation of ECM environment during axonal growth and NMJ development, Neurosci. Lett. 724 (2020), 134822, https://doi.org/10.1016/j.neulet.2020.134822.

[37] A. Kumar, J.K. Placone, A.J. Engler, Understanding the extracellular forces that determine cell fate and maintenance, Development 144 (23) (2017) 4261–4270, https://doi.org/10.1242/dev.158469.

[38] T. Gordon, Peripheral nerve regeneration and muscle reinnervation, Int. J. Mol. Sci. 21 (22) (2020), https://doi.org/10.3390/ijms21228652.

[39] W. Adidharma, A.N. Khouri, J.C. Lee, et al., Sensory nerve regeneration and reinnervation in muscle following peripheral nerve injury, Muscle Nerve 66 (4) (2022) 384–396, https://doi.org/10.1002/mus.27661.

[40] K.L. Wofford, R.B. Shultz, J.C. Burrell, et al., Neuroimmune interactions and immunoengineering strategies in peripheral nerve repair, Prog. Neurobiol. 208 (2022), 102172, https://doi.org/10.1016/j.pneurobio.2021.102172.

[41] Y. Sakai, M. Tsunekawa, K. Ohta, et al., The integrin signaling network promotes axon regeneration via the src-ephexin-RhoA GTPase signaling Axis, J. Neurosci. 41 (22) (2021) 4754–4767, https://doi.org/10.1523/jneurosci.2456-20.2021.

[42] C.L. Xiao, W.C. Yin, Y.C. Zhong, et al., The role of PI3K/Akt signalling pathway in spinal cord injury, Biomed. Pharmacother. 156 (2022), 113881, https://doi.org/10.1016/j.biopha.2022.113881.

[43] M. Chatterjee, K. Li, L. Chen, et al., Gbx2 regulates thalamocortical axon guidance by modifying the LIM and Robo codes, Development 139 (24) (2012) 4633–4643, https://doi.org/10.1242/dev.086991.

[44] M. Wagner, J. Lévy, S. Jung-Klawitter, et al., Loss of TNR causes a nonprogressive neurodevelopmental disorder with spasticity and transient opisthotonus, Genet. Med. 22 (6) (2020) 1061–1068, https://doi.org/10.1038/s41436-020-0768-7.

[45] R.S. Smith, M. Florio, S.K. Akula, et al., Early role for a Na(+),K(+)-ATPase (ATP1A3) in brain development, Proc. Natl. Acad. Sci. U.S.A. 118 (25) (2021), https://doi.org/10.1073/pnas.2023333118.

[46] S. Wang, C. Zhu, B. Zhang, et al., BMSC-derived extracellular matrix better optimizes the microenvironment to support nerve regeneration, Biomaterials 280 (2022), 121251, https://doi.org/10.1016/j.biomaterials.2021.121251.

[47] Y. Qian, X. Zhao, Q. Han, et al., An integrated multi-layer 3D-fabrication of PDA/RGD coated graphene loaded PCL nanoscaffold for peripheral nerve restoration, Nat. Commun. 9 (1) (2018) 323, https://doi.org/10.1038/s41467-017-02598-7.

[48] Y. Qian, H. Lin, Z. Yan, et al., Functional nanomaterials in peripheral nerve regeneration: scaffold design, chemical principles and microenvironmental remodeling, Mater. Today 51 (2021) 165–187, https://doi.org/10.1016/j.mattod.2021.09.014.

[49] L. Zhan, J. Deng, Q. Ke, et al., Grooved fibers: preparation principles through electrospinning and potential applications, Adv. Fiber Mater. 4 (2022) 203–213, https://doi.org/10.1007/s42765-021-00116-5.